




# Light-induced enhancement of memory effect in self-assembled pyrene nanostructures

Arup Ghorai<sup>1</sup>, Rabaya Basori<sup>1,\*</sup>, Anupam Midya<sup>1,\*</sup>, and Samit K. Ray<sup>2,\*</sup> 

<sup>1</sup>School of Nanoscience and Technology, Indian Institute of Technology Kharagpur, Kharagpur 721302, India

<sup>2</sup>Department of Physics, Indian Institute of Technology Kharagpur, Kharagpur 721302, India

Received: 7 June 2021

Accepted: 13 October 2021

Published online:

3 January 2022

© The Author(s), under exclusive licence to Springer Science+Business Media, LLC, part of Springer Nature 2021

## ABSTRACT

A one-pot self-assembly method for the growth of one-dimensional nanoribbons of pyrene with high yield is reported. Nitric acid-treated pyrene molecules are self-assembled to form nanoribbons at room temperature. Morphological structure, composition, crystallinity and functionality of nitric acid-treated pyrene have been studied by electron microscopy, X-ray diffraction, X-ray photoelectron spectroscopy, energy-dispersive X-ray spectroscopy and Fourier transform infrared spectroscopy. A significant modification in optical absorption and properties is observed in pyrene nanoribbons as compared to pristine pyrene. Electrical resistive switching in dark and under illumination is observed in single pyrene nanoribbons down to 100 nm width and length determined by deposited nanoelectrodes of spacing  $\sim 500$  nm, for the first time. Almost a four-order enhancement in ON/OFF switching current ratio is observed under illumination compared to that of dark, paving the way for small molecular nanoassembly-based light-controlled memory devices in future.

## Introduction

In recent years, nanostructures of small-molecular organic materials have attracted much attention for the development of novel optoelectronic devices due to their low cost production over a large area, large number of variety, ease of functionalization, mechanically flexible devices via molecular design and tuneable electronic and optical properties. Among them, one-dimensional (1D) organic

semiconductor wires are currently in use as building blocks for various electronic and optical applications such as field effect transistors[1] [2], light-emitting diodes[3], photo-switches[4], vapour sensors[5] and optical waveguides[6][7]. A number of methods including re-precipitation, solvent evaporation[8], physical/chemical vapour deposition[9], template-assisted growth[10] and electrospinning technique[11] have been employed to grow organic micro-/nanostructures of different morphologies.

Handling Editor: Andrea de Camargo.

Address correspondence to E-mail: rabaya@iitkgp.ac.in; anupam.midya@iitkgp.ac.in; anumidya@gmail.com; physkr@phy.iitkgp.ac.in

Self-assembly is one of the techniques, generally employing solvent exchange or non-solvent nucleation methods, to grow 1D organic nanowires or nanorods[8] [12]. In this method, large amount of molecules are transferred from a saturated solution into a relatively poor solvent to induce supersaturation. The facet-dependent surface free energy leads to the growth of molecules in one direction to form nanoribbons or nanowires. However, controlling the morphology and size in self-assembly of conjugated organic molecules is a major challenge and aggregation during self-assembly for the growth of organic nanostructure is one of them. Driving forces for self-assembly are based on different intermolecular forces like van der Waals interaction, hydrogen bonding, coordination bonding, hydrophobic interaction,  $\pi$ - $\pi$  stacking, etc. Aromatic molecules generally stack through  $\pi$ - $\pi$  interaction, which leads to the formation of 1D nanostructure by self-assembly. This  $\pi$ -stacking greatly depends on the degree of functionalization of oligoacenes. Interestingly, transistors fabricated employing these organic nanostructures showed high carrier mobility[13].

Presently, several groups have prepared benzothiadiazole or benzoselenadiazole derivatives linked with different electron donor units and studied their properties[14][15][16]. But, there are very few reports on 1D nanostructures (e.g. nanowires) synthesized from pyrene. Zhang et al. [17] have synthesized organic nanowire of different aspect ratio by the self-assembly method using sodium dodecyl sulfonate micelles as template and studied their optical properties. Feng et al. [18] have synthesized different functional group-substituted pyrene nanostructures and studied their optical properties. Formation of 1D structure in the self-assembly method is of high interest to researchers in developing novel nanostructure materials.

Here, in this report, we have grown nitric acid-induced pyrene nanoribbons of 2–6 microns in length and width of around 100 nm using an easy and cost-effective way. The nitric acid-treated pyrene nanoribbons show attractive optical properties with photoresponse over a broad spectral range. Although there are very few results on electrical resistive state switching of pyrene-based materials[19–21], till date, no report has been found on light-controlled resistive switching in pyrene nanostructures. We have observed the light-induced resistive switching characteristics for the first time using pyrene

nanoribbons. A four-order enhancement of ON/OFF switching current ratio is observed under the illumination, and the possible mechanism of transport is discussed with the support of band energy diagram. This report manifests pyrene nanostructure potentially attractive for flexible light-controlled organic memory devices in future.

## Experimental

### Synthesis of pyrene nanoribbon

Ten milligrams of pyrene (purity 99%) purchased from Merck was solubilized in 10 ml of 70% HNO<sub>3</sub> by stirring for 30 min to obtain a yellow transparent solution. The mixture was then stirred for 30 min at 60 °C until it became reddish brown. Thereafter, the reaction mixture was allowed to settle for 12 h at room temperature. The precipitate was separated by centrifugation at 10,000 rpm for 10 min. This centrifugation process was repeated several times with DI water to remove excess acid to reach the pH of supernatant 7. Then, the resultant precipitate was dried in an oven overnight at 60 °C at ambient atmosphere. It was then solubilized into acetone for further characterization and device fabrication. A stepwise synthesis process is presented in Fig. 1.

**Electrochemical characterizations:** Cyclic voltammetry (CV) of as-synthesized pyrene nanoribbons was performed using a Gamry potentiostat (Model no: Interface1000). Tetrabutylammonium hexafluorophosphate (TBAPF<sub>6</sub>, 0.1 M) was used as an electrolyte. Pt disc, Ag/AgCl, 3 M KCl and Au were used as the working, reference and counter electrodes, respectively. The CV curve was measured in chlorobenzene solution at a scan rate of 20 mV/s within the window range of 0 to 1.5 V. The highest occupied molecular orbital energy level was calculated from the oxidation onset potential (0.87 V) using the following equation:

$$E_{\text{HOMO}} = -[E_{\text{onset}}(\text{OX}) + 4.8 - E_{\text{FOC}}] \quad (1)$$

where  $E_{\text{onset}}(\text{OX})$  is the onset oxidation potential of pyrene nanoribbon, 4.8 is the reference energy level of ferrocene (FOC, 4.8 eV below the vacuum level) and  $E_{\text{FOC}}$  is the potential of FOC/FOC<sup>+</sup> vs. Ag/AgCl (0.42 eV, as measured by cyclic voltammetry).  $E_{\text{LUMO}}$  was calculated using the following equation:

$$E_{\text{LUMO}} = E_{\text{HOMO}} + E_{\text{g}} \quad (2)$$

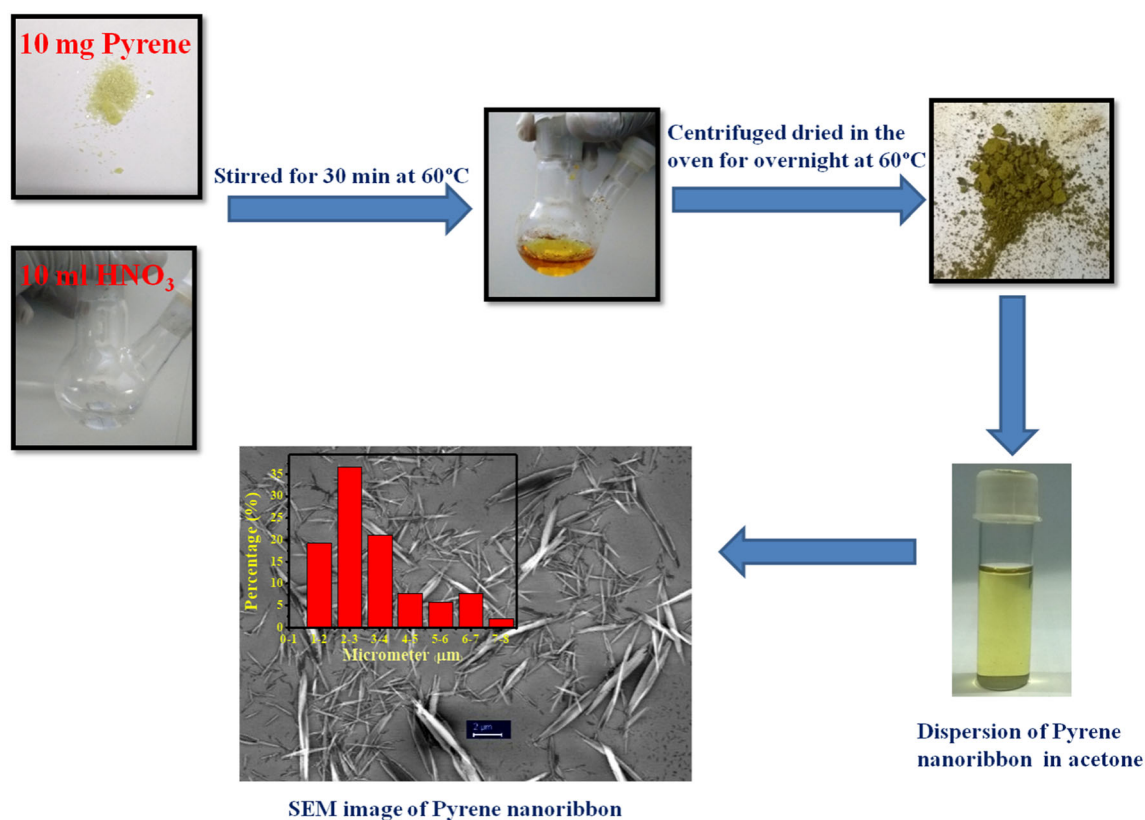


**Figure 1** Schematic of pyrene nanoribbons growth by solution-based self-assembly method and FESEM micrograph along with the size histogram of synthesized pyrene nanoribbons.

where  $E_{\text{HOMO}}$  and  $E_{\text{LUMO}}$  are the HOMO and LUMO energy levels and  $E_g$  is the optical bandgap of the material.

**Device Fabrication:** For electrical characterization of the synthesized pyrene nanoribbons, we have fabricated nanodevices on interdigitated electrodes with specific spacing using a two-step lithography process, i.e. electron beam lithography in combination with photolithography. In the first step, larger electrodes of Cr (10 nm)/Au (100 nm) were made by photolithography process and were used to connect them with the external electronic circuit. In the second step, smaller electrodes of the same metals with desired electrode spacing were fabricated using electron beam lithography process and were linked to the electrodes made in the first step. Pyrene-based nanoribbons were then dispersed on the lithographically fabricated electrodes to connect them between the electrodes. The length of the pyrene nanoribbons connected by dispersing on predefined electrodes is determined by the electrode spacing. In this paper, we have reported two different devices D-1 and D-2 with different electrode spacing. Figure 2a shows the

schematic diagram of predefined electrodes fabricated by a two-step lithography process, and Fig. 2b (i) and (ii) shows the field emission scanning electron

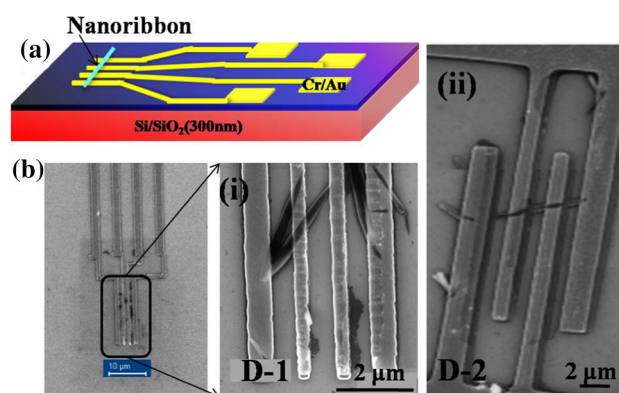


**Figure 2** a Schematic diagram of fabricated predefined electrodes made by electron beam lithography process. b FESEM image of the device. Magnified image shows pyrene nanoribbons connected between two consecutive electrodes, (i) few no. of nanoribbons connected between electrodes with spacing  $\sim 0.5 \mu\text{m}$  and (ii) single nanoribbon connected between electrodes with spacing  $\sim 1.3 \mu\text{m}$ .

microscopy (FESEM) image of dispersed pyrene nanoribbons on predefined electrode of spacing  $\sim 0.5 \mu\text{m}$  (D-1) and  $\sim 1.3 \mu\text{m}$  (D-2), respectively. Electrical characterizations were carried out through the current–voltage characteristics using a Keithley 4200-SCS semiconductor characterization system at ambient in a probe station.

## Results and discussion

### Physical characterization

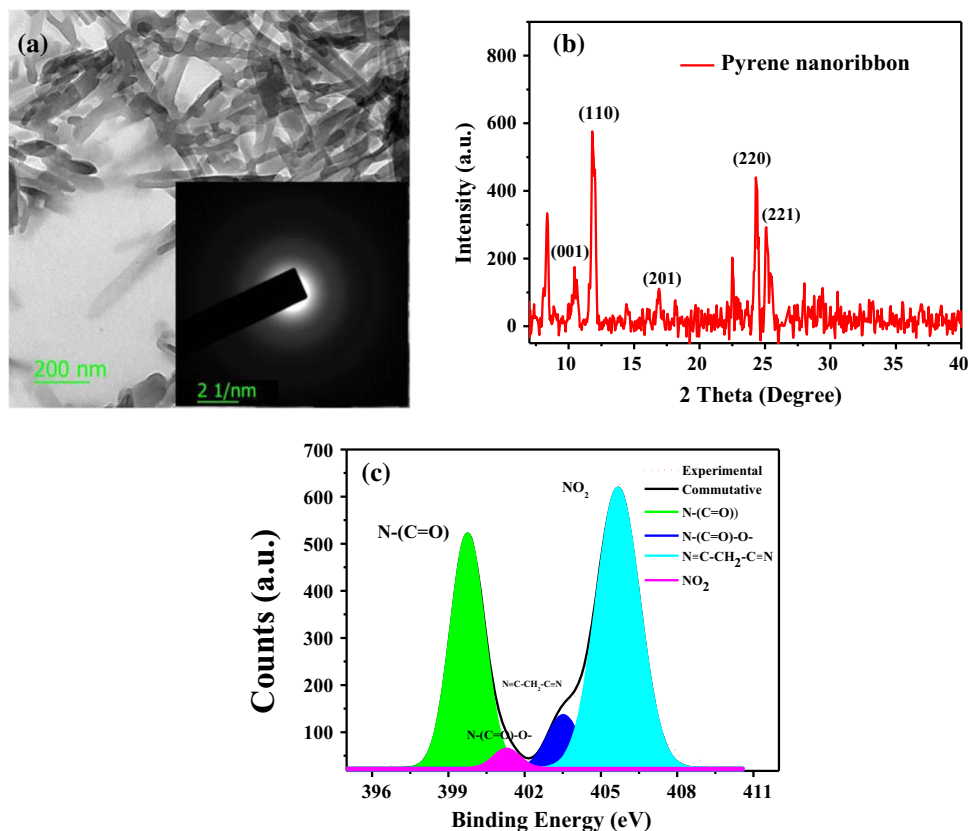
FESEM image and the corresponding histogram of the pyrene nanostructures shown in Fig. 1 clearly confirm the formation of nanoribbons having a length of 2–6 microns and diameter of  $\sim 100 \text{ nm}$ .

Transmission electron spectroscopy (TEM) image of pyrene nanostructures is shown in Fig. 3a, which corroborates the SEM results on nanoribbon morphology. The selected area electron diffraction (SAED) pattern indicates the amorphous nature of pyrene nanoribbons (inset of Fig. 3a). However, interestingly, it shows diffraction peaks in X-ray diffraction pattern, as shown in Fig. 3b, indicating the

polycrystalline nature of pyrene nanoribbon. Therefore, the irradiation of high-energy electron beam (200 kV operating voltage), during TEM measurement, may cause the transformation of pyrene molecules from crystalline to amorphous phase [22] detected in the SAED pattern. All peaks in the XRD pattern are identified by ICDD No. 00–024–1855 for pyrene. The peaks at  $24.3^\circ$  and  $25.1^\circ$  indicate the linear alignment of the planes parallel to the surface. On the other hand, peaks corresponding to (110) and (220) planes indicate the direction of the top face along the (110) plane [23].

Further, to analyse the composition of pyrene nanoribbons, X-ray photoelectron spectroscopy (XPS) of as-synthesized pyrene nanoribbon has been acquired. High-resolution XPS spectrum of N1s of pyrene nanoribbon in Fig. 3c shows two intense peaks, one at 399.7 eV and the other at 405.6 eV. The peak at 399.7 eV is attributed to the N–C=O functional group, and the peak at 405.6 eV is due to  $\text{NO}_2$  functional group, respectively. Along with these main two peaks, there are several other peaks due to different nitrogen functionalizations of pyrene moiety.

**Figure 3** **a** TEM image of as-synthesized pyrene nanoribbons. Inset shows the SAED pattern on a single nanoribbon **b** XRD pattern of the as-synthesized pyrene nanoribbons shows polycrystalline nature **c** X-ray photoelectron spectrum of N 1 s of nitric acid-treated pyrene nanoribbon.



For further confirmation of the presence of different elements in the pyrene nanoribbon, we have performed energy-dispersive spectrometry (EDS) and observed the presence of nitrogen in addition to carbon and oxygen in the organic nanoribbon (Fig. 4a). As shown in Fig. 4a, as-synthesized pyrene nanoribbon contains substantial amount of nitrogen (11.5% atom) leading to the surface functionalization.

To get further insight into the functional group present in the pyrene, we have performed Fourier transform infrared (FTIR) spectroscopy, and the results are displayed in the spectrum shown in Fig. 4b. FTIR spectrum of pyrene nanoribbon shows an absorption peak at  $1182.6\text{ cm}^{-1}$ , corresponding to the vibrational mode of C–N bonds. There are also two prominent absorption peaks at 1340 and  $1589.7\text{ cm}^{-1}$  responsible for vibrational N–O bonds for symmetric and asymmetric stretching, respectively.

### Optical Properties

UV–visible absorption spectra of the pyrene nanoribbons dispersed in acetone (1 mg/ml) are shown in Fig. 5a. The characteristic absorption peaks of pyrene nanoribbons appear at 407 and 584 nm, whereas pristine pyrene before nitric acid treatment shows a strong absorption peak at 280–295 nm, attributed to the vibronic feature of pure pyrene molecules. This higher energy absorption of the pristine pyrene sample is attributed to the intramolecular  $\pi\text{-}\pi^*$  absorption [18]. More interestingly, following nitric acid treatment, the absorption edge is shifted towards a higher wavelength and is broadened as well. This redshift of the absorption band suggests a reordering of the aromatic framework. The strong absorption peak at around 350 nm indicates the aggregation of pyrene molecule. Zhang

et al. have proposed that for long nanowire the absorption peak becomes prominent compared to nanoparticles [17] and the trailing edge of the spectra also becomes more pronounced due to the Mie scattering effect [24]. More interestingly the absorption peak broadens after nitric acid treatment, which is attributed to the extended delocalization of  $\pi$ -electrons over the large area of the molecule [25]. That is the reason why the optical density of absorption band as well as the band gap decreases in the case of pyrene nanoribbon due to extended conjugation.

We have studied photoluminescence of both pristine (bulk) and pyrene nanoribbons. The pristine (bulk) pyrene in acetone (1 mg/ml) shows a strong and broad excimer emission in the range 420 to 550 nm under the excitation of 376 nm source, which is shown in Fig. 5b. Pyrene shows two emission peaks, one in the range of 370–410 nm due to monomer emission and the other at 420–500 nm due to excimer emission. In our study, for pyrene, the emission from monomer is substantially suppressed by the excimer emission, whereas the spectrum of the pyrene nanoribbons in acetone shows a broad emission from 400 to 650 nm with an extra prominent emission peaks at 537 nm and another at 621 nm. The peak at 537 nm is due to the excimer emission, and the peak at 621 nm is due to the intramolecular charge transfer band of pyrene nanoribbons. The optical band gap of pyrene nanoribbon is calculated to be 2.8 eV from the Tauc plot shown in Fig. 5c.

The HOMO and LUMO energy levels of as-synthesized pyrene nanoribbons were calculated from cyclic voltammetry (CV) measurement. The CV curve in Fig. 5d shows a well-distinguished oxidation peak within the voltage range of 0 to 1.5 V. The calculated ONSET of the peak is 0.87 V. Therefore, the  $E_{\text{HOMO}}$  is calculated to be  $-5.25\text{ eV}$ , using Eq. (1). Using the

**Figure 4** a EDS and b FTIR spectrum of pyrene nanoribbon.

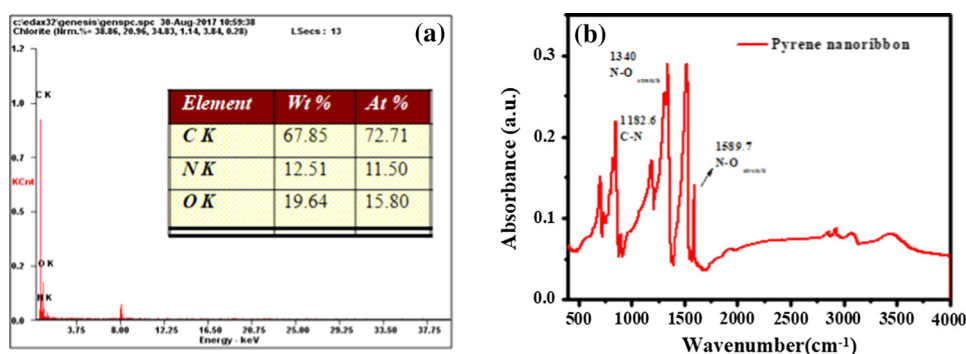
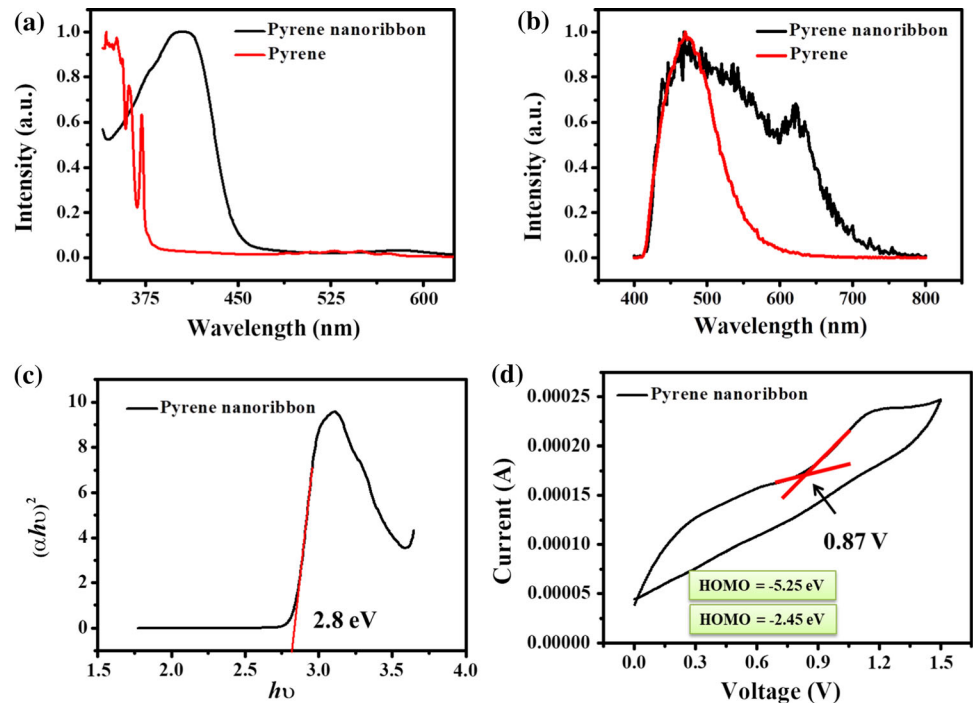


**Figure 5** **a** Absorption spectra of pure pyrene and pyrene nanoribbons; **b** photoluminescence spectra of pristine and pyrene nanoribbons under an excitation wavelength of 376 nm; **c** Tauc plot of as-synthesized pyrene nanoribbon; **d** CV curve of as-synthesized pyrene nanoribbon. HOMO and LUMO levels are calculated from CV curve and Tauc plot using Eqs. 1 and 2.



optical band gap of pyrene nanoribbon, the  $E_{\text{LUMO}}$  is calculated to be  $-2.45$  eV from Eq. (2).

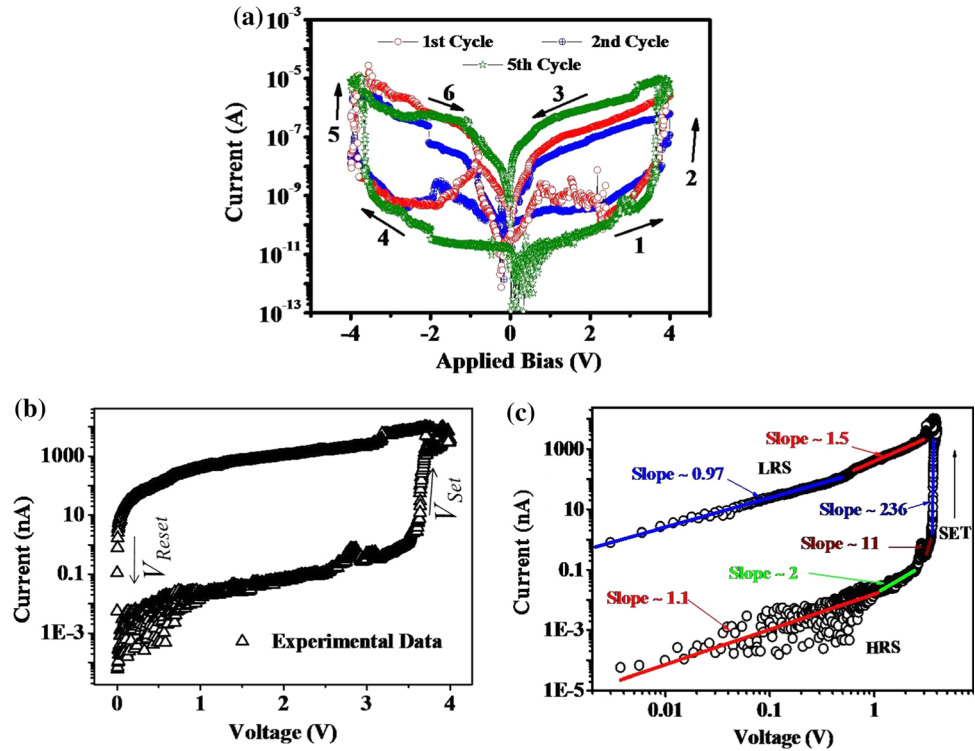
### Electrical Properties

Electrical measurement was taken from two devices with different nanoribbon lengths (for electrical measurement, electrode spacing defines the nanoribbon length): D-1 with length  $l = 0.5 \mu\text{m}$  and D-2 with length  $l \sim 1.3 \mu\text{m}$ . Voltage is applied and current is measured across the nanoribbons with a Keithley 4200-SCS semiconductor characterization system. During measurement, operating voltage and current compliance were restricted to 0 to  $\pm 4$  V and  $10 \mu\text{A}$ , respectively, for D-1 and 0 to  $+10$  V and  $100 \mu\text{A}$ , respectively, for D-2 to bypass possible device breakdown. The voltage and current compliance limits for two devices are set two distinct values due to dissimilar nanoribbon length.

The I–V characteristics of the device D-1 for multiple cycles are shown in Fig. 6. All measurements were taken at room temperature and ambient atmosphere. The voltage bias was scanned as  $0 \rightarrow +4 \rightarrow 0 \rightarrow -4$  V, and the semi-logarithmic plot of the I–V up to fifth cycles is presented in Fig. 6a, which clearly shows hysteresis behaviour for both forward and reverse bias. This hysteresis behaviour is attributed to the charge trapping and detrapping in

the defect states of active materials, which contribute to the memory effect. A double-logarithmic I–V characteristic for the first positive half cycle is presented in Fig. 6b. The pyrene nanoribbon-based memory device is initially in the high resistive state (HRS), and the bias voltage varying from 0 to  $+4$  V is applied externally. The device remained in its HRS during the positive voltage sweep, and at  $\sim 3.5$  V, it switches from HRS to low resistive state (LRS), with the corresponding voltage defined as  $V_{\text{Set}}$  or  $V_{\text{th}}$  and electric field as  $E_{\text{Set}}$  or  $E_{\text{thr}}$  where  $E_{\text{Set}} = V_{\text{Set}}/l$ ,  $l$  being the length of the nanoribbon connected between two consecutive electrodes. During high to low voltage sweep, the device maintained its LRS and at  $\sim 0$  V the device switches back to HRS. The voltage at which it changes its state from LRS to HRS is called  $V_{\text{Reset}}$ , and the corresponding field is called  $E_{\text{Reset}}$ . The electrical transport phenomena like switching depend on threshold field ( $E_{\text{Set}}/E_{\text{Reset}}$ ) and not on the voltage ( $V_{\text{Set}}/V_{\text{Reset}}$ ) applied across the material. So, the same material with larger electrode spacing may require higher voltage to get switching. The same type of RHS and LHS state is observed for reverse bias too. One important parameter to use a device as a memory is ON/OFF current or voltage ratio, which clearly distinguishes between ‘0’ and ‘1’ states suppressing the effect of noise. The ON/OFF current ratio of pyrene nanoribbon-based resistive switching

**Figure 6** a I–V characteristics of the pyrene nanoribbon-based memory device (D-1) in semi-logarithmic scale measured with repeated voltage scan ( $V = \pm 4$  V) up to the fifth cycle. **b** Semi-logarithmic I–V curve for positive first cycle only. **c** Double logarithmic of the same, illustrating the gradient values of linear fitted curves.



device reported here is quite high ( $I_{ON}/I_{OFF} \sim 10^4$ ). The possible reason of superior ON/OFF ratio is due to the single layer of pyrene, which creates a well-defined interface between donor and acceptor molecules. On the other hand, multi-layer is known to create randomness due to excess boundary of donor acceptor molecules, which reduces current. The observation of electrical resistive switching in such organic small molecular nanostructure is new and needs a detailed study. We have checked the reproducibility of switching behaviour in multiple devices.

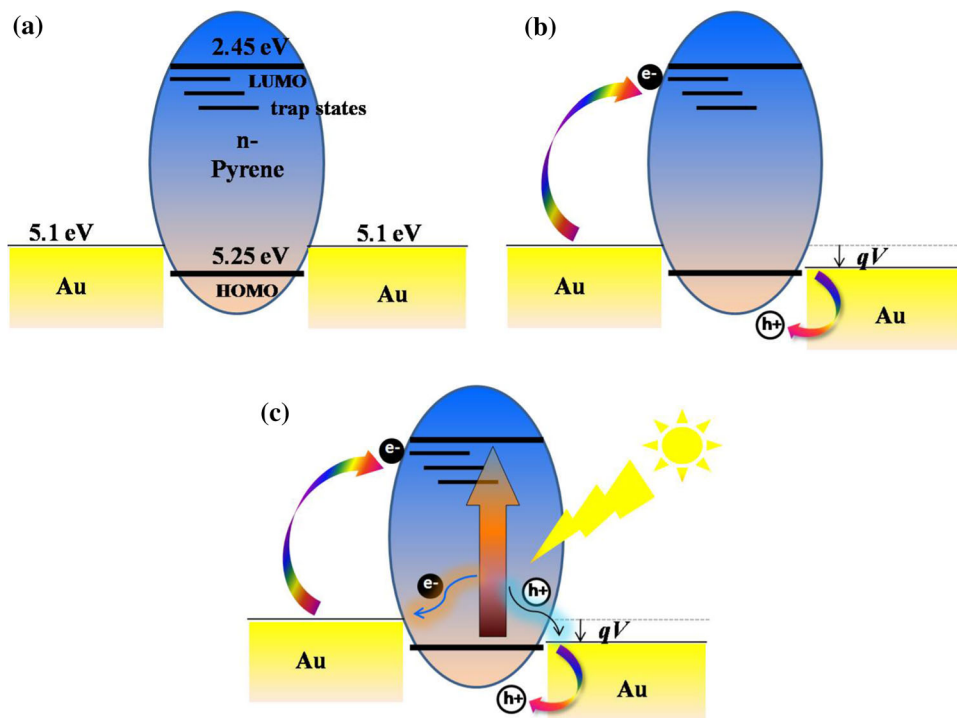
**Conduction mechanism**

Several approaches have been presented to explain the switching mechanisms of organic non-volatile resistive switching memory devices in the studies. Conduction mechanism in these devices can be attributed to trapping and detrapping of charge carriers due to the externally applied electric field [26, 27]. It implies that when the traps are fully occupied by charge carriers, the device switches from HRS to LRS at an applied bias of  $V_{Set}$  or field  $E_{Set}$  and in order to bring it back to HRS, all the filled traps must be emptied by applying a voltage ( $V_{Reset}$ ) or field  $E_{Reset}$ . One important point to note that it is not the applied bias, but the electric field across the

electrodes which determines the transition from HRS to LRS ( $E_{Set}$ ) or from LRS to HRS ( $E_{Reset}$ ) [28].  $E_{Reset}$  could be of the same or opposite polarity of  $E_{Set}$  polarity depending on the nature of switching, i.e. it is unipolar or bipolar [29]. Unipolar trapping and detrapping occurs with the same polarity of applied voltage. Bipolar detrapping occurs with polarity opposite to that of trapping voltage [26]. In our case,  $E_{Reset}$  (close to zero) is of the same polarity with  $E_{Set}$  signifying unipolar resistive switching in this material. This implies that with increasing field, the charge carriers start filling the trap states and once these states are filled completely at the applied field  $E_{Set}$ , a sudden jump in the current value is observed. This indicates the transition of the device from HRS to LRS. During retracing the applied field from higher to a lower value, the device maintains its LRS above  $E_{Reset}$  field. Once the applied field reaches below  $E_{Reset}$  (Fig. 6b), the trap charges are detrapped again and the system gets back to its HRS. This trapping and detrapping at two different voltages lead to a hysteresis in the I–V curve. Similar hysteresis loop is observed for the negative cycle also.

The conduction mechanism taking place in our device (D1) is well supported by double logarithmic linear fitting I–V curves, as shown in Fig. 6c. The HRS region can be fitted by the three curves with different

**Figure 7** Schematic representation of conduction mechanism in different conditions. **a** Band diagram of the MSM device in thermal equilibrium, **b** mechanism of switching under applied bias, **c** the photocarrier generation and transport under illumination.



slopes, which signify that the conduction mechanism of the memory device can be explained by trap-controlled space-charge-limited current (TCSCLC) model. TCSCLC consists of multi-regions separated by different slope values of the linear fitting plot, i.e. the ohmic region (slope  $\sim 1$ ), the Child's law region (slope  $\sim 2$ ) and a region of sharp current increase (slope  $> 230$ ) [27]. Initially, at a low voltage due to the thermally generated charge carriers, the ohmic conduction behaviour dominates (slope of 1.1). With increasing voltage, charge carriers kept on increasing and begin to fill empty traps. The space charge effects are dominant, and the current-voltage behaviour follows a quadratic nature (slope of 2). In this region,

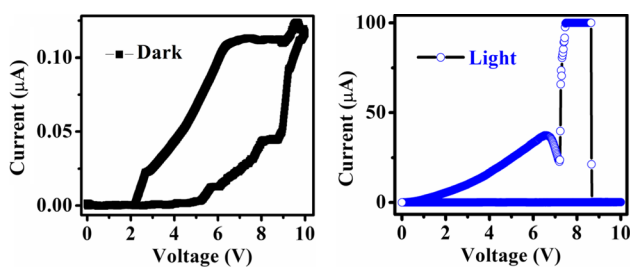


**Figure 8** Semi-logarithmic I–V curve of another pyrene nanoribbon-based memory devices in the dark as well as under illumination. No significant change in switching voltage is observed, whereas the current for low resistive state (LRS) increases to almost  $10^3$  times under illumination.

the injected charge carriers fill the traps in the pyrene nanoribbons. At a specific value of applied voltage known as  $V_{Setr}$ , the available traps are completely filled with charge carriers, resulting in an exponential increase in current ( $I \propto V^m$ ), where the exponent  $m$  is  $\sim 236$ . Following this transition, almost all the traps with higher mobility are occupied by charge carriers, turning the device into LRS, where it is again governed by ohmic conduction, as suggested by the slope value (slope of  $\sim 1.5$ – $0.97$ ) from the double logarithmic curve in Fig. 6c.

The above mechanism can also be explained by the energy band diagram of the device, as illustrated schematically in Fig. 7. With the device under test, pyrene nanoribbon is connected between Au electrodes, the work function of which is  $\sim 5.1$  eV. Pyrene nanoribbon has HOMO and LUMO value of  $\sim 5.25$  eV and  $\sim 2.45$  eV, respectively, as obtained from the Tauc plot (Fig. 5c) and CV curve (Fig. 5d) and well supported to the value of past report [28]. Band alignment of the device in thermal equilibrium is shown in Fig. 7a. Depending on the polarity of applied bias, pyrene will act as a donor or acceptor. The HOMO value of pyrene being lower is almost close to the work function of Au; charge will flow from Au to pyrene HOMO. On the other hand, the charges will flow from pyrene LUMO to Au when



**Table 1** Device performance in dark and under illumination conditions

Device	Nanoribbon length ( $\mu\text{m}$ )	$V_{\text{th}}$ (Volt)	$E_{\text{th}}$ (Volt/cm)	ON/OFF current ratio
D-1	0.5	3.5	$7 \times 10^4$	$10^4$
D-2	1.3	9	$6.9 \times 10^4$	$10^3$ (Dark)
		9	$6.6 \times 10^4$	$10^7$ (Illuminated)

bias is applied through the device as illustrated in Fig. 7b.

### Tuning of resistive switching under illumination

As pyrene nanoribbons show strong optical absorption (Fig. 4a), we have also investigated resistive switching under illumination using another device (D2) (electrode spacing  $\approx$  nanoribbon length  $\sim 1.3 \mu\text{m}$ ) and compared it with dark characteristics of the same. Along with Keithley 4200-SCS semiconductor characterization system, a broadband solar simulator (AM 1.5,  $100 \text{ mW}/\text{cm}^2$ ) light was used as an illumination source. Figure 8a represents the resistive switching in the dark with ON/OFF ratio  $\sim 10^3$  and is closer to the results as obtained in device D-1. Although there is no change in the resistive threshold field under dark and illumination, significant improvement is observed in the ON current (LRS current) under illumination, as shown in Fig. 8b, and ON/OFF ratio is enhanced to  $\sim 10^7$ . Almost same value has been observed in other functional pyrene-based resistive devices reported recently [19–21]. We have observed almost four order of increase in LRS current, when the device is illuminated with light. This large light-induced enhancement of LRS current is attributed to the additional photogenerated charge carriers under illumination. Photogenerated electron–hole pairs in pyrene nanoribbon are collected by the Au electrodes before recombination due to tiny electrode gap. Table 1 summarizes the performance of the D-1 and D-2 devices in the dark as well as under illumination. The device D-2 is switched to LRS at  $\sim 9 \text{ V}$ , whereas switching occurred in D-1 at  $\sim 3.5 \text{ V}$ . This is due to larger electrode spacing ( $\sim 1.3 \mu\text{m}$ ) in D-2 compared to D-1 (electrode spacing  $\sim 0.5 \mu\text{m}$ ), and to get required field of switching which is constant for a material, higher voltage is applied in device D-2.

Under illumination, photocarriers are generated in the pyrene nanoribbons and collected to the consecutive electrodes by the applied field across the

nanoribbons. Photogenerated electrons and holes are accelerated to the Au electrodes by the externally applied electric fields. Since the pyrene nanoribbons are connected individually without creating any junction in between two electrodes, it acts like a cleaner and smoother conduction path for carriers, which reduce the possibility of scattering or any other effect that can interrupt carrier transport. This results in a reduction in device current. Additionally, trap charges also get ejected by absorbing light and promote to the enormous enhancement in device current. Moreover, electrode separation is small ( $1.3 \mu\text{m}$ ); almost all the photogenerated carriers are collected by the electrodes before recombinations which contribute to the huge enhancement in device current under illumination, as illustrated in Fig. 7c. Although large enhancement in ON current is observed under illumination, it does not have any influence on resistive switching field as in other inorganic materials like Pd/Al<sub>2</sub>O<sub>3</sub>/SiO<sub>2</sub>/Si[32], Ag/NiWO<sub>4</sub>/Ti[33] and ITO/ZnO/TiO[34] devices reported earlier. Our study reveals that the improved performance of resistive state switching property under illumination may open up future research possibilities for electrical as well as optoelectronic applications.

### Conclusions

In summary, we have grown pyrene nanoribbons using a simple one-pot synthesis technique and investigated the optical and electrical characteristics. Detailed characterizations reveal the formation of polycrystalline pyrene nanoribbon. Resistive switching characteristics are observed in pyrene-based nanoribbons deposited on predefined interdigitated electrodes with  $\sim$  micron spacing. The ON/OFF ratio in resistive switching is found to be  $\sim 10^4$  with a low operating voltage of  $\sim 3.5 \text{ V}$  in these small molecular organic nanostructure devices, which are comparable to those using inorganic switching layers. The resistive switching behaviour is explained by the

conduction mechanism of TCSCLC in HRS and ohmic conduction in LRS. The ON/OFF current ratio is significantly improved ( $\sim 4$  order) under illumination, compared to the dark, attributed to the photogenerated carriers participating in conduction. The superior resistive switching property with light-controlled tunability in pyrene nanoribbon opens up possibility of using organic nanostructures as light-controlled memory devices as well as optoelectronic devices in near future.

## Acknowledgements

The authors gratefully acknowledge DST, Govt. of India, for financial support (NNetRA project). AM acknowledges DST for Inspire Faculty project Grant No. IFA 13-MS-09, and RB acknowledges DST for Inspire Faculty project Grant No. IFA-15-MS-70.

## Funding

This work is funded by DST, Govt. of India.

## Declarations

**Conflict of interest** The authors declare that they have no conflict of interest.

## References

- [1] Cui Y, Zhong Z, Wang D et al (2003) High performance silicon nanowire field effect transistors. *Nano Lett* 3:149–152. <https://doi.org/10.1021/nl025875l>
- [2] Zhang X, Ju W, Gu M et al (2005) A facile route to fabrication of inorganic–small organic molecule cable-like nanocomposite arrays. *Chem Commun* 4202. <https://doi.org/10.1039/b506459g>
- [3] Curran SA, Ajayan PM, Blau WJ et al (1998) A Composite from Poly(m-phenylenevinylene-co-2,5-dioctoxy-p-phenylenevinylene) and carbon nanotubes: a novel material for molecular optoelectronics. *Adv Mater* 10:1091–1093. [https://doi.org/10.1002/\(SICI\)1521-4095\(199810\)10:14%3c1091::AID-ADMA1091%3e3.0.CO;2-L](https://doi.org/10.1002/(SICI)1521-4095(199810)10:14%3c1091::AID-ADMA1091%3e3.0.CO;2-L)
- [4] Nau S, Wolf C, Sax S, List-Kratochvil EJW (2015) Organic non-volatile resistive photo-switches for flexible image detector arrays. *Adv Mater* 27:1048–1052. <https://doi.org/10.1002/adma.201403295>
- [5] Che Y, Yang X, Liu G et al (2010) Ultrathin n-type organic nanoribbons with high photoconductivity and application in optoelectronic vapor sensing of explosives. *J Am Chem Soc* 132:5743–5750. <https://doi.org/10.1021/ja909797q>
- [6] Greytak AB, Barrelet CJ, Li Y, Lieber CM (2005) Semiconductor nanowire laser and nanowire waveguide electro-optic modulators. *Appl Phys Lett* 87:1–3. <https://doi.org/10.1063/1.2089157>
- [7] Zhao YS, Peng A, Fu H et al (2008) Nanowire waveguides and ultraviolet lasers based on small organic molecules. *Adv Mater* 20:1661–1665. <https://doi.org/10.1002/adma.200800123>
- [8] Xiao J, Xiao X, Zhao Y et al (2013) Synthesis, physical properties and self-assembly behavior ofazole-fused pyrene derivatives. *Nanoscale* 5:5420. <https://doi.org/10.1039/c3nr00523b>
- [9] Geometry MFT, Catenanes G, Equilibrium ML (1999) Controlled growth and electrical properties of heterojunctions of carbon nanotubes and silicon nanowires. *Nature* 399:48–51. <https://doi.org/10.1038/19941>
- [10] Tan LK, Chong ASM, Tang XSE, Gao H (2007) Combining atomic layer deposition with a template-assisted approach to fabricate size-reduced nanowire arrays on substrates and their electrochemical characterization. *J Phys Chem C* 111:4964–4968. <https://doi.org/10.1021/jp066841v>
- [11] Lin DD, Wu H, Pan W (2007) Photoswitches and memories assembled by electrospinning aluminum-doped zinc oxide single nanowires. *Adv Mater* 19:3968–3972. <https://doi.org/10.1002/adma.200602802>
- [12] Park DH, Kim MS, Joo J (2010) Hybrid nanostructures using  $\pi$ -conjugated polymers and nanoscale metals: synthesis, characteristics, and optoelectronic applications. *Chem Soc Rev* 39:2439. <https://doi.org/10.1039/b907993a>
- [13] Briseno AL, Mannsfeld SCB, Reese C et al (2007) Perylenediimide nanowires and their use in fabricating field-effect transistors and complementary inverters. *Nano Lett* 7:2847–2853. <https://doi.org/10.1021/nl071495u>
- [14] Velusamy M, Thomas KRJ, Lin JT et al (2005) Organic dyes incorporating low-band-gap chromophores for dye-sensitized solar cells. *Org Lett* 7:1899–1902. <https://doi.org/10.1021/ol050417f>
- [15] İçli M, Pamuk M, Algi F et al (2010) Donor-acceptor polymer electrochromes with tunable colors and performance. *Chem Mater* 22:4034–4044. <https://doi.org/10.1021/cm100805g>
- [16] Guo X, Qin C, Cheng Y et al (2009) White electroluminescence from a phosphonate-functionalized single-polymer system with electron-trapping effect. *Adv Mater* 21:3682–3688. <https://doi.org/10.1002/adma.200803734>

- [17] Zhang X, Zhang X, Shi W et al (2005) Morphology-controllable synthesis of pyrene nanostructures and its morphology dependence of optical properties. *J Phys Chem B* 109:18777–18780. <https://doi.org/10.1021/jp052385j>
- [18] Feng X, Hu JY, Yi L et al (2012) Pyrene-based Y-shaped solid-state blue emitters: synthesis, characterization, and photoluminescence. *Chem - An Asian J* 7:2854–2863. <https://doi.org/10.1002/asia.201200530>
- [19] Ren Y, Chang C-L, Ting L-Y et al (2019) Flexible Pyrene/Phenanthro[9,10-d]imidazole-based memristive devices for mimicking synaptic plasticity. *Adv Intell Syst* 1:1900008. <https://doi.org/10.1002/aisy.201900008>
- [20] Barman BK, Guru MM, Panda GK et al (2019) Pyrene-affixed triazoles: a new class of molecular semiconductors for robust, non-volatile resistive memory devices. *Chem Commun* 55:4643–4646. <https://doi.org/10.1039/C8CC10185J>
- [21] Wang H, Zhou F, Wu L et al (2018) An all-in-one memory cell based on a homopolymer with a pyrene side chain and its volatile and nonvolatile resistive switch behaviors. *Polym Chem* 9:1139–1146. <https://doi.org/10.1039/C7PY01925D>
- [22] Grubb DT (1974) Radiation damage and electron microscopy of organic polymers. *J Mater Sci* 9:1715–1736. <https://doi.org/10.1007/BF00540772>
- [23] Ibe S, Ise R, Oaki Y, Imai H (2012) Twisted growth of organic crystal in a polymer matrix: Sigmoidal and helical morphologies of pyrene. *CrystEngComm* 14:7444–7449. <https://doi.org/10.1039/c2ce26079d>
- [24] Auweter H, Haberkorn H, Heckmann W et al (1999) Supramolecular structure of precipitated nanosize beta-carotene particles. *Angew Chem Int Ed Engl* 38:2188–2191. [https://doi.org/10.1002/\(SICI\)1521-3773\(19990802\)38:15%3c2188::AID-ANIE2188%3e3.0.CO;2-#](https://doi.org/10.1002/(SICI)1521-3773(19990802)38:15%3c2188::AID-ANIE2188%3e3.0.CO;2-#)
- [25] Thomas KRJ, Lin JT, Tao YT, Chuen CH (2002) Green and yellow electroluminescent dipolar carbazole derivatives: Features and benefits of electron-withdrawing segments. *Chem Mater* 14:3852–3859. <https://doi.org/10.1021/cm0202512>
- [26] You T, Du N, Slesazek S et al (2014) Bipolar electric-field enhanced trapping and detrapping of mobile donors in BiFeO<sub>3</sub> memristors. *ACS Appl Mater Interfaces* 6:19758–19765. <https://doi.org/10.1021/am504871g>
- [27] Wang H, Meng F, Cai Y et al (2013) Sericin for resistance switching device with multilevel nonvolatile memory. *Adv Mater* 25:5498–5503. <https://doi.org/10.1002/adma.201301983>
- [28] Basori R, Samanta S (2018) Diameter dependent threshold voltage modification of resistive state switching in organometallic single nanowire devices (diameter ~ 10–100 nm). *Appl Phys Lett* 113:123507. <https://doi.org/10.1063/1.5033970>
- [29] Basori R, Kumar M, Raychaudhuri AK (2016) Sustained resistive switching in a single Cu:7,7,8,8-tetracyanoquinodimethane nanowire: a promising material for resistive random access memory. *Sci Rep* 6:1–12. <https://doi.org/10.1038/srep26764>
- [30] Rehman MM, Yang BS, Yang YJ et al (2017) Effect of device structure on the resistive switching characteristics of organic polymers fabricated through all printed technology. *Curr Appl Phys* 17:533–540. <https://doi.org/10.1016/j.cap.2017.01.023>
- [31] Jeon NJ, Lee J, Noh JH et al (2013) Efficient inorganic-organic hybrid perovskite solar cells based on pyrene arylamine derivatives as hole-transporting materials. *J Am Chem Soc* 135:19087–19090. <https://doi.org/10.1021/ja410659k>
- [32] Ungureanu M, Zazpe R, Golmar F et al (2012) A light-controlled resistive switching memory. *Adv Mater* 24:2496–2500. <https://doi.org/10.1002/adma.201200382>
- [33] Sun B, Zhao W, Wei L et al (2014) Enhanced resistive switching effect upon illumination in self-assembled NiWO<sub>4</sub> nano-nests. *Chem Commun* 50:13142–13145. <https://doi.org/10.1039/C4CC05784H>
- [34] Shih CC, Chang KC, Chang TC et al (2014) Resistive switching modification by ultraviolet illumination in transparent electrode resistive random access memory. *IEEE Electron Device Lett* 35:633–635. <https://doi.org/10.1109/LED.2014.2316673>

**Publisher's Note** Springer Nature remains neutral with regard to jurisdictional claims in published maps and institutional affiliations.